Spectrochimica Acta Part A: Molecular and Biomolecular Spectroscopy 310 (2024) 123972

Contents lists available at ScienceDirect

Spectrochimica Acta Part A: Molecular and Biomolecular Spectroscopy

journal homepage: www.journals.elsevier.com/spectrochimica-acta-part-a-molecular-and-biomolecular-spectroscopy

Rational construction of MOF derived α-Fe_2O_3/g-C_3N_4 composite for effective photocatalytic degradation of organic pollutants and electrocatalytic oxygen evolution reaction

Sakthivel Kumaravel [a,*,1], Balakrishna Avula [b], Chandramoorthy Chandrasatheesh [c,1], Theophile Niyitanga [a,*], Rajasekar Saranya [d], Imran Hasan [e], T. Abisheik [f], Rajakumar S. Rai [g], V. Pandiyan [f], Krishnakumar Balu [h,i,*]

[a] School of Materials Science and Engineering, Yeungnam University, Gyeongsan 38541, Republic of Korea
[b] Department of Chemistry, Rajeev Gandhi Memorial College of Engineering and Technology (Autonomous), Nandyal, Andhra Pradesh 518501, India
[c] Department of Chemistry, Loyola College, Chennai 600034, Tamil Nadu, India
[d] Department of Biotechnology, SRM Institute of Science and Technology, Ramapuram, Chennai 600089, Tamil Nadu, India
[e] Department of Chemistry, College of Science, King Saud University, Riyadh 11451, Saudi Arabia
[f] Department of Physics, Nehru Memorial College (Autonomous), Puthanampatti (Affiliated to Bharathidasan University), Tiruchirappalli 621007, Tamil Nadu, India
[g] Division of Mechanical Engineering, Karunya Institute of Technology and Sciences, Karunya Nagar, Coimbatore 641114, Tamil Nadu, India
[h] Saveetha School of Engineering, Saveetha Institute of Medical and Technical Sciences (SIMATS), Chennai 602105, Tamil Nadu, India
[i] Departamento de Ingeniería y Ciencia de los Materiales y del Transporte, E.T.S. de Ingenieros, Universidad de Sevilla, Avda. Camino de los Descubrimientos s/n., 41092 Sevilla, Spain

HIGHLIGHTS

- Bare GCN, Fe_2O_3, and FGCN materials were synthesized by thermal polymerization and hydrothermal methods.
- FGCN photocatalyst exhibited excellent performance in RhB and CV degradation under solar irradiation.
- FGCN catalyst exhibited excellent catalytic performance in OER.
- The composite catalyst showed good stability.

GRAPHICAL ABSTRACT

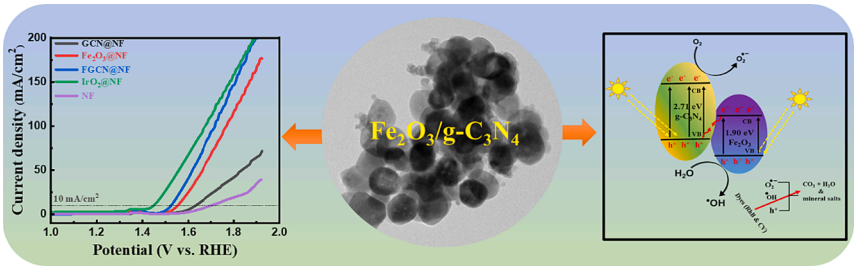

ARTICLE INFO

Keywords:
Fe_2O_3/g-C_3N_4
Photocatalysts
Rhodamine B
Crystal violet
OER

ABSTRACT

In recent years, researchers have been actively investigating metal oxide-based materials with narrow bandgaps due to their potential applications toward wastewater treatment and oxygen evolution reactions (OER). In this study, we successfully synthesized g-C_3N_4 (GCN), Fe_2O_3, and Fe_2O_3/g-C_3N_4 (FGCN) using thermal polymerization and hydrothermal methods. We characterized the physicochemical and structural properties of these materials through various analytical techniques including XRD, FT-IR, UV-DRS, XPS, FE-SEM, and HR-TEM analyses, confirming the effective construction of the FGCN composite catalyst. We evaluated the photocatalytic activity of Fe_2O_3, GCN, and FGCN composite catalysts by assessing their ability to degrade rhodamine B (RhB)

* Corresponding authors at: Departamento de Ingeniería y Ciencia de los Materiales y del Transporte, E.T.S. de Ingenieros, Universidad de Sevilla, Avda. Camino de los Descubrimientos s/n., 41092 Sevilla, Spain.
E-mail addresses: sakthiveltm1992@gmail.com (S. Kumaravel), t.niyitanga@yu.ac.kr (T. Niyitanga), kbalu@us.es (K. Balu).
[1] These authors equally contributed.

https://doi.org/10.1016/j.saa.2024.123972
Received 24 November 2023; Received in revised form 20 January 2024; Accepted 27 January 2024
Available online 1 February 2024

and crystal violet (CV) by exposing them to sunlight for 150 min. Among these catalysts, the FGCN composite demonstrated excellent photocatalytic performance, achieving 93 % and 95 % degradation of RhB and CV, respectively, under 150 min of sunlight exposure. The developed Fe_2O_3/g-C_3N_4@Nickel foam (FGCN@NF) composite catalyst exhibits remarkable OER performance, with a reduced Tafel slope of 64 mV/dec and a low overpotential of 290 mV at a current density of 10 mA/cm^2 and shows excellent durable performance over a long time (15 h). Total Organic Carbon (TOC) analysis confirmed the mineralization of both dyes. The photocatalytic performance remained largely unchanged after five consecutive experiments, demonstrating excellent reusability and photostability. Trapping experiments revealed that $O_2^{\bullet-}$ is the main species responsible for the photocatalytic decomposition of various dyes by the FGCN composite catalyst. Therefore, the development of a versatile photo/electrocatalytic system that can efficiently promote energy conversion in environmental applications has attracted great attention.

1. Introduction

Over the past century, the rapid increase of industrial activities worldwide has highlighted the serious impact of environmental pollution on public health. Among these most important issues, water pollution has emerged as a major environmental issue, with a particular focus on the contamination of wastewater by dyes originating from industries such as textiles, printing, dyeing, leather, food, and cosmetics [1,2]. Synthetic dyes are generally not effectively removed by common wastewater treatment processes, leading to their release into the environment [3]. This persistence can have long-term effects on the organisms that inhabit the ecosystem [3]. Among the numerous synthetic dyes used in the textile industry, including methylene blue, congo red, rhodamine, crystal violet, methyl orange, and malachite green, rhodamine B (RhB) and crystal violet (CV) are the most widely used [4]. RhB and CV are widely used in the textile industry and are very popular [5]. The textile industry releases approximately 280,000 tons of dye into the environment worldwide each year, creating significant environmental problems [6]. Therefore, there is a strong need to address this problem by exploring ways to degrade various pollutants, which are highly beneficial to society. One of the most promising approaches to address these issues is the use of semiconductor-based photocatalytic technologies that can harness solar or visible light energy [7]. It is of utmost importance to find reliable ways to effectively remove various environmental pollutants from surface waters using sunlight as a natural energy source [8].

Fossil fuel depletion and associated climate change caused by industrialization and human activities are pressing global issues. As a result, advances in clean energy technology have become important, and water electrolysis for hydrogen production has emerged as a promising green and renewable option [9]. One promising solution is the use of hydrogen production through water electrolysis. This method involves two key reactions: oxygen evolution at the anode and hydrogen evolution at the cathode [10]. Both reactions require the use of cost-effective and efficient electrocatalysts. Nevertheless, the OER exhibits high overpotentials and slow reaction kinetics, highlighting the urgent need to develop electrocatalysts that can significantly increase the reaction rate and overcome the energy barrier. Currently, noble metal oxides such as RuO_2 and IrO_2 serve as high performance for electrocatalysts [11]. However, limited reserves, poor stability, and high costs for large-scale applications intended to look at another material [11]. To address this challenge, researchers have focused on designing transition metal oxide-based electrocatalysts that are not only cost-effective and efficient but also stable and readily available [12]. One particularly important aspect is the development of electrocatalysts that exhibit low overpotentials, allowing for more efficient clean energy production.

In recent years, extensive research has focused on exploring the potential of transition metal oxides to degrade organic dyes and promote electrocatalytic OER reactions. Various metal oxides have been studied, including ZnO, WO_3, MoO_4, MOS_2, Fe_2O_3, Fe_2O_4, TiO_2, Co_3O_4, MnO_2 and WS_2 [13–15]. Hematite (Fe_2O_3) is a widely occurring iron oxide that exhibits excellent absorbance in the visible light spectrum, offers various oxidation states and coordination environments, is economically viable, non-toxic, extremely stable, highly reliable, resistant to corrosion, and possesses a narrow band gap width of 2.1 eV [16–18]. However, it has been observed that pure Fe_2O_3 has poor photocatalytic and electrochemical performance [19]. On the bright side, the researchers were able to increase the catalytic performance of Fe_2O_3 by combining it with other catalysts to form a heterojunction.

In recent years, there has been a growing interest in the non-metallic semiconductor graphitic carbon nitride (GCN) [20]. This material is widely used in photocatalytic and electrochemical OER reactions due to its many advantages such as narrow bandgap, exceptional thermal and chemical stability, non-toxicity, and electron conductivity, making it an excellent material for photocatalysis and electrochemical OER reactions [21]. However, it also has some drawbacks, such as rapid charge recombination rate, limited visible light utilization ability, and reduced charge transfer ability to the catalyst surface, which ultimately limits the photocatalytic and electrocatalytic performance [22]. In contrast, single-phase semiconducting metal oxides face unique challenges, including limited availability of sunlight and visible light, faster charge carrier recombination, and limited charge transfer capacity. To address these limitations, various methods have been explored to improve the performance of photocatalytic and electrochemical OER, including the creation of heterojunctions by combining two or more materials.

The extensive utilization of FGCN composites in heterojunction fabrication is due to their exceptional photocatalytic and electrochemical performance, structural controllability, affordability, rapid photoinduced charge transfer, reduced recombination rate, and robust redox ability. Fe-based materials can form heterojunctions with GCN, leading to enhanced photocatalytic and electrochemical OER performance. Notable examples include TiO_2/Fe_2O_3/g-C_3N_4 [23], Fe_2O_3/g-C_3N_4/GO [24], α-Fe_2O_3/g-C_3N_4 [17], α-Fe_2O_3/CdS/g-C_3N_4 [25], g-C_3N_4/Fe_2TiO_5/Fe_2O_3 [26], and TiO_2/Fe_2O_3 [27], RuO_2–Fe_2O_3/HrGO [28], Fe_2O_3/FeP [29], Er-MOF/Fe_2O_3 [30], and, Fe_2O_3@CNT [31] composites all exhibit improved photocatalytic and electrochemical OER performance. Among these, composites of g-C_3N_4 and Fe_2O_3 stand out for their responsiveness to sunlight, stability, and ease of preparation. A significant method to increase the effectiveness of bare Fe_2O_3 includes the development of heterostructures with GCN, which enhances the photo/electrocatalytic performances through improvements in parameters such as band structure, electron-hole separation, and surface area.

In this study, we used thermal polymerization and hydrothermal methods to synthesize GCN, Fe_2O_3, and FGCN composite heterostructures to improve the catalytic performance for both photocatalysis and electrochemical OER. A physicochemical method was utilized to verify the phase formation, surface morphology, and formation of heterostructures. We evaluated the photocatalytic activity for the degradation of organic dyes RhB and CV under sunlight exposure and showed that the optimized FGCN composite photocatalyst has outstanding performance. Moreover, the FGCN showed excellent reusability in multiple cycles of dye removal. For the degradation of RhB and CV, the FGCN heterostructure showed the highest rate constant. The as-developed FGCN@NF composite catalyst reveals remarkable oxygen evolution reaction (OER) performance. Additionally, we also discussed a possible Z-

scheme mechanism to degrade RhB and CV dyes using the fabricated FGCN composite catalyst.

2. Experimental section

2.1. Materials

Analytical grade of iron(III) nitrate nonahydrate ($Fe(NO_3)_3{\cdot}9H_2O$), N,N- dimethylformamide (DMF, 99.8 % purity), terephthalic acid (98 % purity), melamine ($C_3H_6N_6$), ethanol (EtOH), were acquired from Sigma-Aldrich. Rhodamine B and crystal violet were obtained from Sisco Research Laboratories Pvt. Ltd. (SRL).

2.2. Fabrication of GCN photocatalyst

Bare GCN photocatalyst was easily formed through a simple thermal polymerization process [32,33]. The general procedure involves placing 2 g of melamine directly into the furnace and heating it at 550 °C for 2 h while keeping it in a covered crucible. After natural cooling to room temperature, the yellow bulk product was collected and ground in a mortar.

2.3. Fabrication of MOF-derived Fe_2O_3 and FGCN catalysts

Fe_2O_3 derived from MOF precursors was successfully synthesized using a previously reported method [34]. In this process, GCN (approximately 50 mg) was dispersed in DMF (20 mL) by sonication for 30 min to form dispersion A. In the next step, 3 mmol of $Fe(NO_3)_3{\cdot}9H_2O$ was added to a beaker containing 30 mL of DMF (solution B). At the same time, 10 mmol terephthalic acid was introduced into another beaker containing 30 mL of DMF (solution C). The sonication process continued until all solids in solutions B and C were completely dissolved. Next, dispersion A, and solutions B, and C were mixed to create mixture D and subjected to sonicated for 60 min. The pH of the reaction mixture was adjusted to a range of 9–10. Finally, solution D was assigned to a 100 mL autoclave and heated at 160 °C for 24 h. After cooling to atmospheric temperature, the solid product was collected by centrifugation, followed by multiple washes with ultrapure water and ethanol. The resulting product was then dried at 70 °C overnight, followed by calcination at 500 °C for 3 h. It is important to note that the preparation of MOF-derived Fe_2O_3 samples was performed using the same method except for the addition of GCN.

2.4. Characterization of materials

The crystalline phase formation and purity of the as-fabricated materials were assessed by X-ray diffraction (XRD) using a (Rigaku Miniflex, Japan). To determine the type of chemical functional groups, present in the materials were assessed by Fourier transform infrared (FT-IR) analysis using a Thermo Fisher iS50 spectrometer. The surface properties of the FGCN most active material were investigated using field emission scanning electron microscopy (FE-SEM/EDS) from (CLARA- Tescan, Czech Republic) and high-resolution transmission electron microscopy (HR-TEM) from (JEOL/JEM-F200). High resolution XPS spectra were measured using (ULVAC–PHI, PHI5000 Version Probe III). To describe the light absorption properties and evaluate the bandgap calculation of the obtained fabricated samples were evaluated by UV–Vis diffuse reflectance spectra (DRS) using a Shimadzu UV-750 spectrophotometer. UV–vis absorption spectra were recorded using a Shimadzu UV-750 spectrophotometer.

2.5. Photocatalytic experiment

The photocatalytic performance of Fe_2O_3, GCN and FGCN materials was evaluated through the degradation of RhB and CV dyes under 150 min of sunlight exposure. First, an aqueous solution containing RhB (20 ppm) and CV (20 ppm) was prepared. In the standard photocatalytic procedure, 100 mL of RhB and CV dye solutions were placed separately in a 150 mL beaker and mixed with 30 mg of photocatalyst. The mixture was then stirred in the dark for 30 min to establish equilibrium between the catalyst and dye solution. Subsequently, the dye solution was irradiated with direct sunlight while being continuously stirred. The sunlight intensity measured by the TES Datalogging solar power meter reached 98 mW/cm^2. Approximately 3 mL of dye solution was collected at various time intervals and then subjected to centrifugation at 5000 rpm for 5 min in order to separate the photocatalyst from the dye solution. UV/Vis absorption spectra were recorded at 30-minute intervals during UV irradiation to monitor changes in dye concentration. Calculations presented in previous studies were used to calculate the degradation rate, apparent rate constant (k_{app}), and half-life period ($t_{1/2}$) [32,33].

2.6. Electrochemical measurements

Electrochemical measurements for the study of OER were conducted using a Biologic SP-150 workstation. Before fabricating the electrode, the nickel foam (NF) underwent a cleaning process with 3 M HCl, acetone, and deionized water using a sonication bath to clean the nickel. The oxide layer on the foam was removed. Subsequently, the washed NF was dried in an oven at 100 °C for 12 h. To fabricate the electrode, 10 mg of the prepared catalyst was dispersed in 480 μL of ethanol along with 20 μL of nafion ionomer solution and sonicated for 30 min to produce a uniform ink. This thick gel was then uniformly coated onto NF (1 × 1 cm^2) and dried at 80 °C for 6 h. The active surface area and mass of the electrodes were 1 cm^2 and 3 mg/cm^2, respectively. All electrochemical experiments took place in a traditional three-electrode cell containing a 1 M KOH alkaline electrode solution saturated with N_2. The counter, reference, and working electrodes were a graphite rod, mercury/mercury oxide (Hg/HgO), and the catalyst-modified NF, respectively. The electrochemical calculation has been given in a supplementary file (see Supporting information).

3. Results and discussion

3.1. Characterization studies

The X-ray diffraction (XRD) patterns of the synthesized materials, including GCN, Fe_2O_3, and FGCN composite, are presented in Fig. 1. The XRD pattern of the synthesized MOF- Fe_2O_3 sample before calcination is

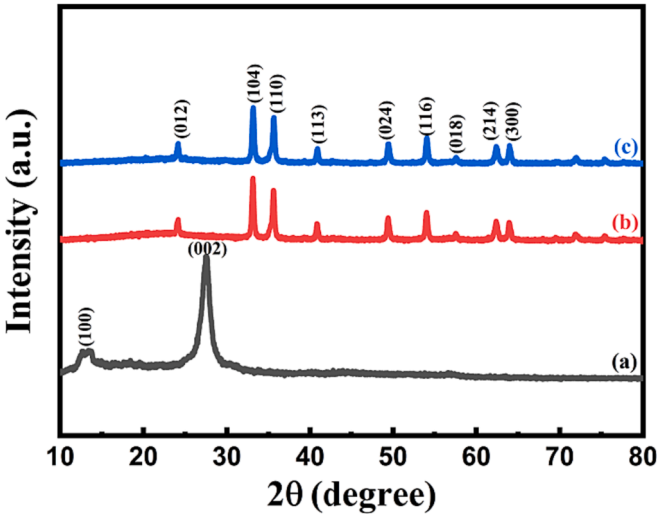

Fig. 1. XRD patterns of the as-synthesized (a) GCN, (b) Fe_2O_3, and (c) FGCN composite materials.

shown in Fig. S1 (see Supporting Information). Fig. S1 shows a prominent XRD diffraction peak at 8.88° for MOF-Fe_2O_3. Remarkably, these diffraction peaks are in good agreement with those reported for MOF-Fe_2O_3 in previous studies [35–38]. The XRD patterns of both Fe_2O_3 and FGCN materials subjected to calcination at 550 °C reveal consistent reflections corresponding to the (012), (104), (110), (113), (024), (116), (018), (214), and (300) planes (Fig. 1). These findings align well with the crystal structure of hematite α-Fe_2O_3, as confirmed by the JCPDS number 79-0007 [39]. These findings indicate the successful crystallization of the prepared samples. Furthermore, the absence of the characteristic MOF peak in the XRD pattern suggests that the organic ligands in the MOF structure were completely decomposed. This observation is in good agreement with the findings described in the previous literature [40]. In the XRD analysis, GCN shows distinct peaks at 12.5° and 27.5°, corresponding to the (100) and (002) planes of the GCN structure, respectively [41]. Furthermore, there is no evidence of peak shifts, suggesting that the crystal structures of Fe_2O_3 and GCN are unaffected after composite formation. The intensity of the characteristic Fe_2O_3 peak decreases slightly with the incorporation of GCN species. However, no clear characteristic peak of GCN is observed in the FGCN composite. This lack can be attributed to the uniform uptake and low-intensity diffraction peaks due to the low concentration of crystalline GCN, which is consistent with previous literature results [32,42,43]. However, the presence of GCN was confirmed with TEM and XPS analyses.

Fig. 2 shows the characteristic functional groups and bond vibrations of the prepared catalysts, including Fe_2O_3, GCN, and FGCN composite catalysts. In the case of Fe_2O_3, two bands are observed at lower wavenumbers, exactly at 426 and 520 cm^{-1}, which can be attributed to the stretching mode of the Fe-O bond [44]. The pristine GCN exhibits three distinctive vibration regions: the first broad band in the range of 3000–3700 cm^{-1} corresponds to stretching vibrations of N–H and O–H bonds [45], while the second region spanning 1210–1640 cm^{-1} is characteristic of the stretching vibrations of C–N and C=N bonds typically found in heterocyclic compounds [46,47]. Furthermore, a sharp peak at 796 cm^{-1} is indicative of the respiration mode of the triazine structure (C-N-C) [47]. Particularly for the FGCN composite, there is no discernible band in the spectrum when the GCN content is low and homogeneous dispersion. The absorption band of the FGCN composite catalyst showed a slight shift to higher wavenumbers. This observation is consistent with findings in previously published literature [48,49].

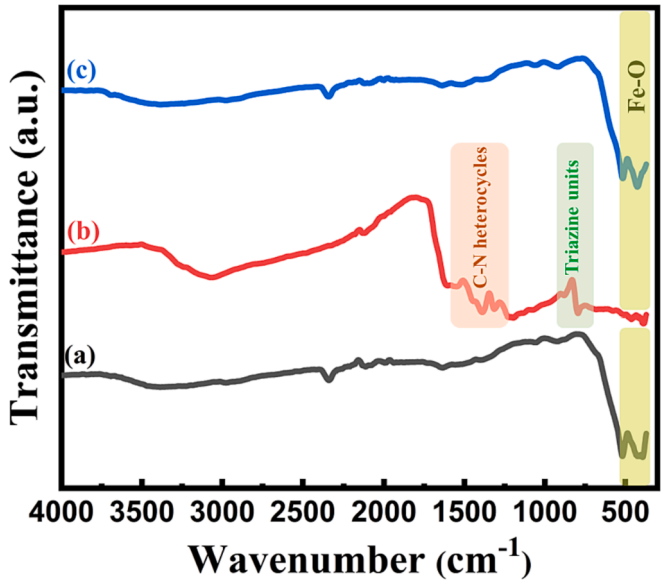

Fig. 2. FT-IR spectra of the as-synthesized (a) Fe_2O_3, (b) GCN, and (c) FGCN composite materials.

Fig. 3 shows the optical properties of the synthesized catalysts Fe_2O_3, GCN, and FGCN were examined using DRS-UV Vis spectroscopy. Fig. 3a-c demonstrates that both pristine and composite catalysts exhibit efficient absorption of visible light. The absorption spectrum of GCN shows a clear edge around 400–500 nm, while Fe_2O_3 shows a broad absorption in the entire visible region, which will be reflected in the FGCN composite. The bandgap energies of the prepared catalysts were determined using the K-M equation, and the corresponding energy spectra are shown in Fig. 3(d-f). After the combination of GCN with Fe_2O_3, the bandgap energy decreases from 1.90 eV (Fe_2O_3) to 1.76 eV (FGCN). The optical bandgap energies of Fe_2O_3, GCN, and FGCN composite catalysts are found to be 1.90, 2.71, and 1.76 eV, respectively. This change in bandgap energy can be attributed to band bending in the semiconductor heterojunction.

The surface morphologies of both Fe_2O_3 and FGCN composite catalysts were examined by FE-SEM, and the corresponding results are demonstrated in Fig. 4a-d. In Fig. 4a and b, the FE-SEM pictures of Fe_2O_3 show a spherical morphology consisting of uniform spheres composed of numerous small nanoparticles. Interestingly, the FGCN composite catalyst (Fig. 4c and d) exhibits a morphology similar to that of Fe_2O_3. This result clearly suggests that the SEM images cannot reveal GCN sheets, probably due to their homogeneous dispersion or the limited amount of GCN used in the composite. Furthermore, no discernible differences in morphological features are evident between pristine Fe_2O_3 and FGCN due to their very small sizes. This morphology is in good agreement with previous literature results [44,50,51]. HR-TEM analysis further confirmed the presence of characteristic spherical shapes of Fe_2O_3 particles uniformly distributed on the GCN surface.

The close association of the FGCN composite catalyst can be easily observed in the TEM and HR-TEM images shown in Fig. 5. These images reveal the characteristic spherical morphology of the FGCN nanostructures as shown in Fig. 5a and b. Moreover, the FGCN composite sample clearly shows a uniform distribution of Fe_2O_3 spheres strongly attached to the GCN surface (marked in red) in Fig. 5 c and g. This results in good agreement with previous literature reports [51–53]. Detailed examination of the surface atomic structure of the as-prepared FGCN nanocomposite samples was carried out using HR-TEM, as evidenced in Fig. 5d and g. As shown in Fig. 5f and k, the well-resolved lattice fringes within the FGCN nanospheres indicate the presence of crystal grains of Fe_2O_3. These observations are consistent with the fast Fourier transform (FFT) patterns and corresponding lattice fringes, as shown in Fig. 5e and j, and are further enhanced by inverse FFT (IFFT) analysis. These analyses revealed interplanar spacings of 0.36 nm and 0.27 nm corresponding to the (012) and (104) planes, confirming the crystal structure of Fe_2O_3 [54]. In Fig. 5g, the enlarged HR-TEM image of FGCN highlights the clear formation of Fe_2O_3 interfacial bonding on the GCN surface. Furthermore, it is clear from Fig. 5i and l that nanointerfaces are formed between the (104) planes of Fe_2O_3, and GCN. The nanointerface junction significantly contributes to catalytic efficiency in both degradation and electrochemical processes.

XPS analysis revealed the electronic and oxidation states of the elements within the highly active FGCN photocatalyst. Fig. 6a displays the survey spectrum, highlighting prominent elements such as C (1s), N (1s), O (1s), and Fe (2p). Within the FGCN composite (Fig. 6b), the C1s spectrum shows two distinct peaks at 284.6 eV and 288.2 eV, corresponding to C=C and N-C=N, respectively [55]. The N 1s spectrum (Fig. 6c) can be deconvoluted into three peaks at 398.5 eV, 399.1 eV, and 400.4 eV, representing (C=N–C), N–$(C)_3$, and C–N–H, respectively. [56,57]. The high-resolution XPS spectrum of O 1s (Fig. 6d) reveals two peaks at 529.5 eV and 531.3 eV, confirming the presence of high-energy lattice metal–oxygen bonds and surface-adsorbed water molecules [58]. Fig. 6e shows the high-resolution Fe 2p spectrum deconvoluted into two peaks. The binding energy of approximately 710.6 eV and 724.2 eV is attributed to Fe $2p_{3/2}$ and Fe $2p_{1/2}$, and the two separate peaks at 709.9 & 711.8 eV and 723.6 & 726.1 eV correspond to Fe^{2+} and Fe^{3+}, respectively [59]. The binding energies of two satellite peaks were

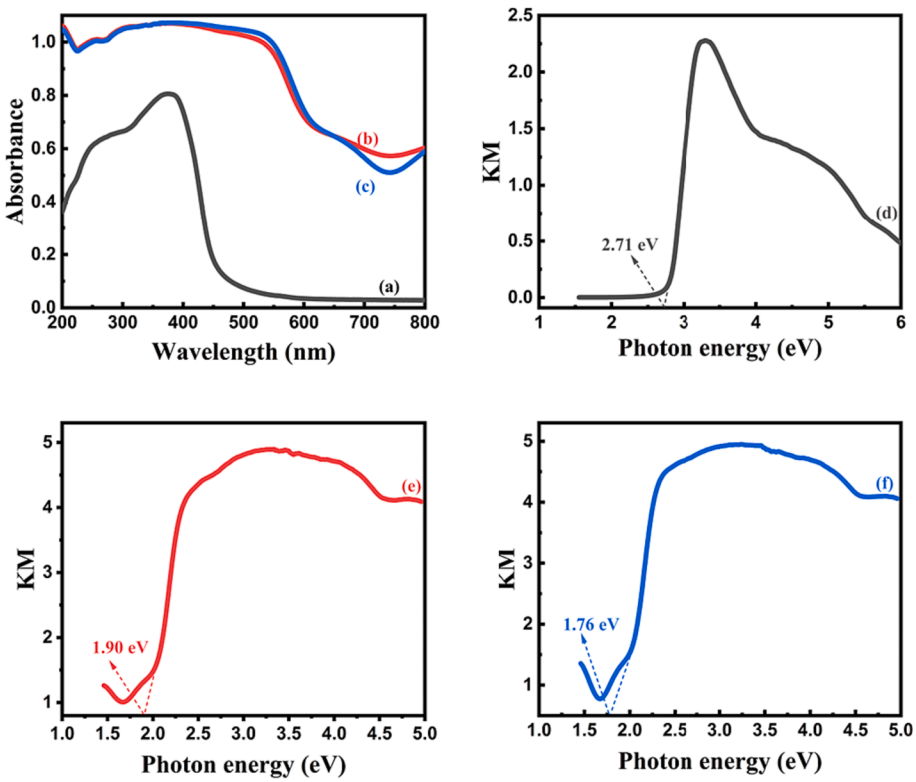

Fig. 3. UV–vis DRS spectra (a) GCN, (b) Fe_2O_3, (c) FGCN, and (d-f) corresponding KM plots of as-prepared catalysts, respectively.

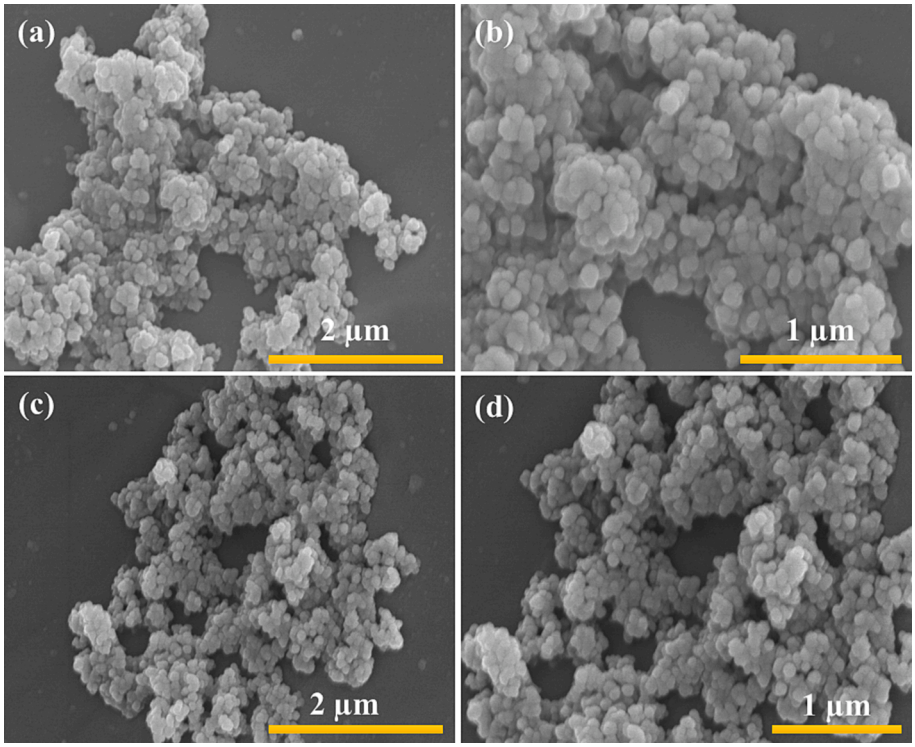

Fig. 4. FE-SEM image of the as-synthesized (a and b) Fe_2O_3, and (c and d) FGCN composite materials.

observed at 718.4 and 732.7 eV, respectively, indicating the presence of Fe^{3+} oxidation states. These findings provide confirmation of the presence of GCN and Fe_2O_3 and establish the formation of an FGCN composite catalyst free of appreciable impurities.

3.2. *Photocatalytic performance*

The photocatalytic degradation efficiency of the materials under investigation was evaluated using RhB and CV organic pollutants in the presence of sunlight. To provide a more comprehensive evaluation of

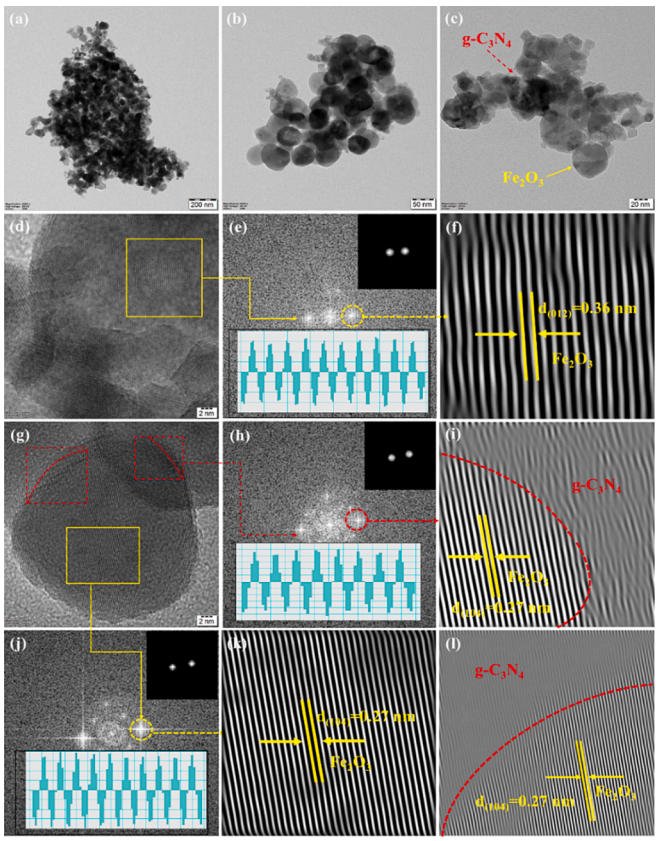

Fig.5. (a–c) TEM images, (d-l) HR-TEM images of FGCN, and its corresponding FFT and IFFT images, and (i, l) FGCN nanointerfaces edges (crystalline planes) stacked on amorphous GCN in the heterostructure nanocomposites.

photocatalytic activity, we carried out degradation experiments of RhB and CV dyes with Fe_2O_3, GCN, and FGCN composite catalysts. The photocatalytic degradation activity curves of these prepared materials are shown in Fig. 7a–d. First, adsorption experiments were performed by stirring the sample for 30 min in the dark to allow the sample to reach adsorption/desorption equilibrium. Notably, without irradiation, only a small portion (5–10 %) of the dye was adsorbed onto the surface of the materials. This indicates that the prepared material has limited adsorption capacity. Fig. 7b and c shows that the light activation capacity of Fe_2O_3 is low, and the degradation rate is only 33 % for RhB dye and 27 % for CV dye when exposed to sunlight. On the other hand, the GCN photocatalyst showed a slight increase in photocatalytic activity and degraded 52 % of RhB and 46 % of CV dyes after 150 min of sunlight exposure. Upon introducing Fe_2O_3 onto the GCN surface, an FGCN composite heterostructure photocatalyst was obtained, which exhibited significantly higher photocatalytic decomposition efficiency (as shown in Fig. 7c and d). This composite catalyst achieved a degradation rate of 93 % for RhB and 95 % for CV organic dyes, outperforming both Fe_2O_3 and GCN under the same conditions. The order of dye decomposition ability of the synthesized photocatalysts can be summarized as FGCN > GCN > Fe_2O_3. The improved photocatalytic efficiency of the FGCN composite catalyst can be attributed to the formation of a heterojunction, which effectively suppresses the rapid recombination of photogenerated electrons and holes. The results clearly demonstrate that the FGCN composite catalyst significantly enhances the decomposition efficiency of both RhB and CV dyes.

As shown in Fig. 7e and f, the data fit well with the classical *pseudo*-first-order kinetic correlation expressed by the equation -ln (C_t/C_0) = t [60]. For both RhB and CV dyes, the Fe_2O_3, GCN, and FGCN photocatalytic degradation rate constants are: 0.00278 min^{-1} & 0.00207 min^{-1}, 0.00483 min^{-1} & 0.00391 min^{-1}, and 0.01973 min^{-1} & 0.02076 min^{-1}, respectively. The k value of RhB dye decomposition in the FGCN composite photocatalytic system (Fig. 7e) is 0.01973 min^{-1}, which is about 7.0 and 4.0 times better than Fe_2O_3 and GCN photocatalysts, respectively. Similarly, the k value of CV dye decomposition in the FGCN composite photocatalyst system (Fig. 7f) was 0.02076 min^{-1}, which was 10.0 and 5.3 times larger than Fe_2O_3 and GCN photocatalysts, respectively. These results clearly demonstrate that the FGCN composite photocatalytic heterostructure significantly enhances the photocatalytic degradation efficiency of both RhB and CV environmental organic pollutants when exposed to solar irradiation.

Evaluation of the photocatalytic efficiency of the fabricated photocatalyst involves tracking the corresponding primary absorption peaks of RhB and CV at 552 nm and 590 nm, respectively. The UV–vis spectra of RhB and MB on the highly effective FGCN composite photocatalyst are shown in Fig. S2a and b, revealing that the maximum absorbance peaks of RhB and MB decrease with time under solar light irradiation. After 150 minutes, both dyes are almost disappearing.

A comprehensive analysis of total organic carbon (TOC) was carried out to evaluate the photocatalytic degradation of RhB and CV dyes in the presence of FGCN composite photocatalyst under solar irradiation (Fig. 8). The experiment included various time intervals extending up to 150 min to observe changes in TOC levels. The results shown in Fig. 8 reveal that the TOC of both RhB and CV dye solutions gradually decreased when subjected to treatment with FGCN composite catalyst during solar exposure. Notably, significant dye mineralization was observed after 150 min of illumination. After this period, the final TOC mineralization rates were recorded at 81 % for RhB and 83 % for CV, respectively. Additionally, this study suggests that the dye can transform into various intermediate forms, [61] and complete mineralization can occur after 150 min. The most active FGCN composite catalyst showing the highest photocatalytic activity was selected to evaluate its applicability to various cationic and anionic dyes. Inspection of Table S1 reveals the remarkable effectiveness of the FGCN photocatalyst in degrading both cationic and anionic dyes under 150 min of sunlight exposure. The details of the degradation kinetics of RhB, CV, CR, MB, and MO dyes using the FGCN composite catalyst are shown in Table S1.

Assessing the reusability of photocatalysts is of great importance in catalysis, especially when considering commercial applications. To further investigate the reusability of the most active photocatalyst the results are depicted in Fig. 9a and b. For each experiment, the most efficient photocatalysts were separated by centrifugation to remove the suspension and then dried at 373 K for 3 h. The photodegradation efficiency of RhB and CV dyes by FGCN catalyst decreased to 82 % and 80 % compared to the initial performance. However, our results clearly show that our catalysts remain stable and reusable for both dyes for up to five consecutive cycles without major changes, confirming their sustained effectiveness. Table S2 shows the recent literature comparison of photocatalytic performance by various Fe-based catalysts.

As shown in Fig.S3, various analytical techniques such as XRD, FE-SEM, and EDX methods were used to characterize the spent photocatalyst. Fig. S3 shows the high angle XRD patterns of both the fresh and used FGCN catalyst. These figures clearly show that even after the fifth run, the spent catalyst shows no noticeable changes compared to the initial FGCN catalyst. Furthermore, Fig. S4a-c shows the FE-SEM images of the spent catalyst after five runs, which shows that the surface morphology structure remains unchanged. Both analyzes collectively verify that the crystal structure and surface morphology of the spent catalyst remain consistent throughout the photocatalytic reaction. EDS and elemental mapping analysis of the spent catalyst is shown in Fig. S4d-i, and shows no significant evidence of elemental leaching during the reaction. This further supports the high stability and durability of the photocatalyst.

In this study, trapping experiments were utilized to investigate the main participants in the photodegradation process when FGCN nanocomposites were exposed to sunlight. The findings are visually represented in Fig. 9c. The introduction of 1 mmol of ammonium oxalate (AO,

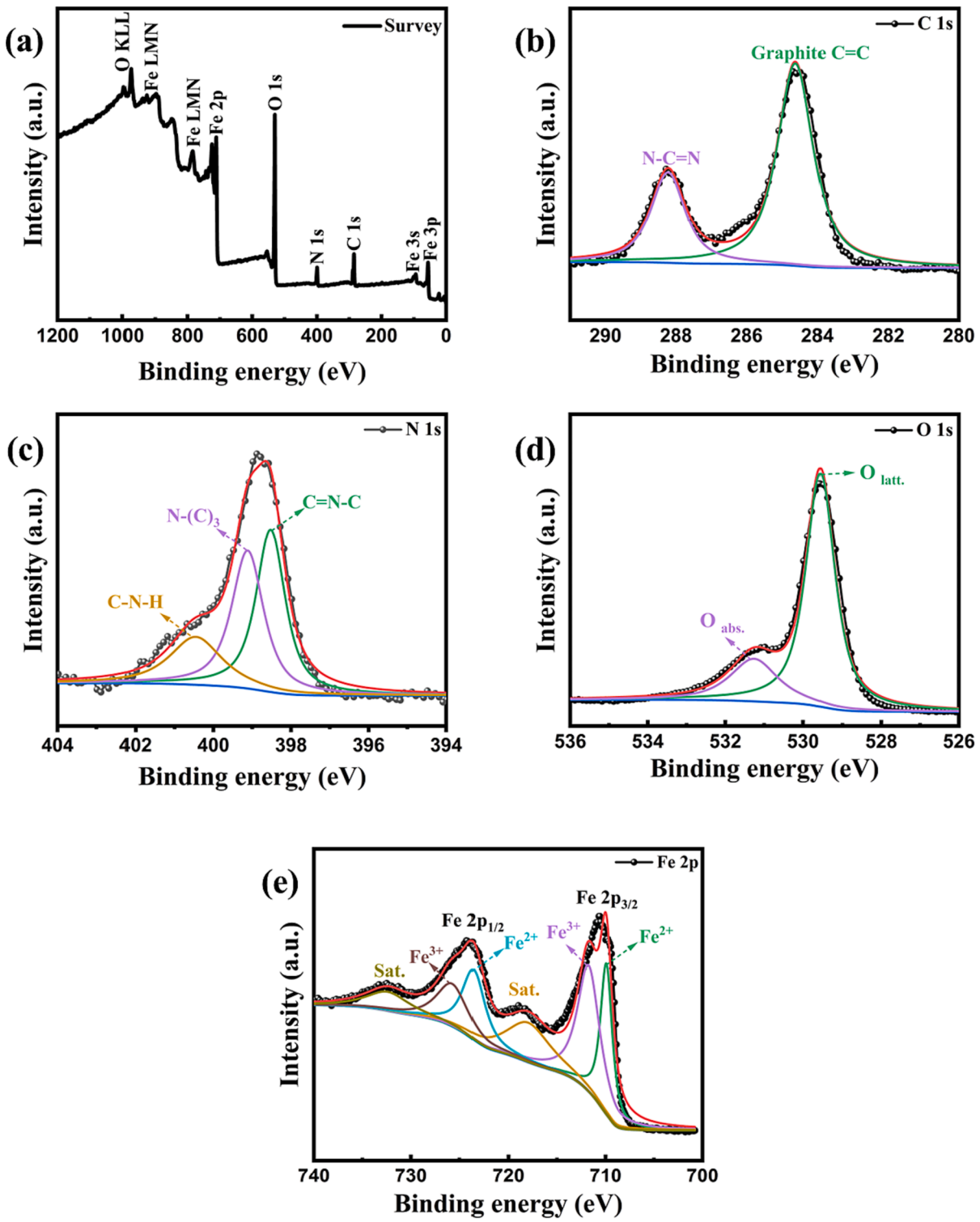

Fig. 6. XPS spectra of the as-synthesized FGCN composite material.

h^+ scavenger), *tert*-butyl alcohol (*t*-BuOH, $^{\bullet}OH$ scavenger), and benzoquinone (BQ, $O_2^{\bullet-}$ scavenger) significantly reduced the photocatalysis efficiency of the catalyst. In the absence of scavengers, approximately 93 % degradation of RhB occurred within 150 min. Conversely, when AO, *t*-BuOH, and BQ were introduced, the degradation rates were 65 %, 47 %, and 33 %, respectively. In particular, BQ had a substantial inhibitory effect on photocatalytic activity, highlighting the importance of $O_2^{\bullet-}$ as the main active species in RhB degradation, followed by $^{\bullet}OH$ and h^+, and are in the following order: $O_2^{\bullet-} > {}^{\bullet}OH > h^+$.

According to the results of UV-DRS studies, the FGCN nanocomposite exhibits a reduced bandgap (1.76 eV) compared to GCN (2.71 eV) and Fe_2O_3 (1.90 eV). Mulliken's electronegativity theory was adopted to determine the conduction band (CB) and valence band (VB) energies of GCN and Fe_2O_3 [62]. Fig. 9d proposes a suitable mechanism for the photocatalytic decomposition of both dyes (RhB and CV) over FGCN under sunlight. The band potentials in GCN are −1.125 eV (CB) and + 1.585 eV (VB), while in Fe_2O_3 they are + 0.42 eV (CB) and + 2.32 eV (VB), respectively. In normal heterojunction arrangement, both

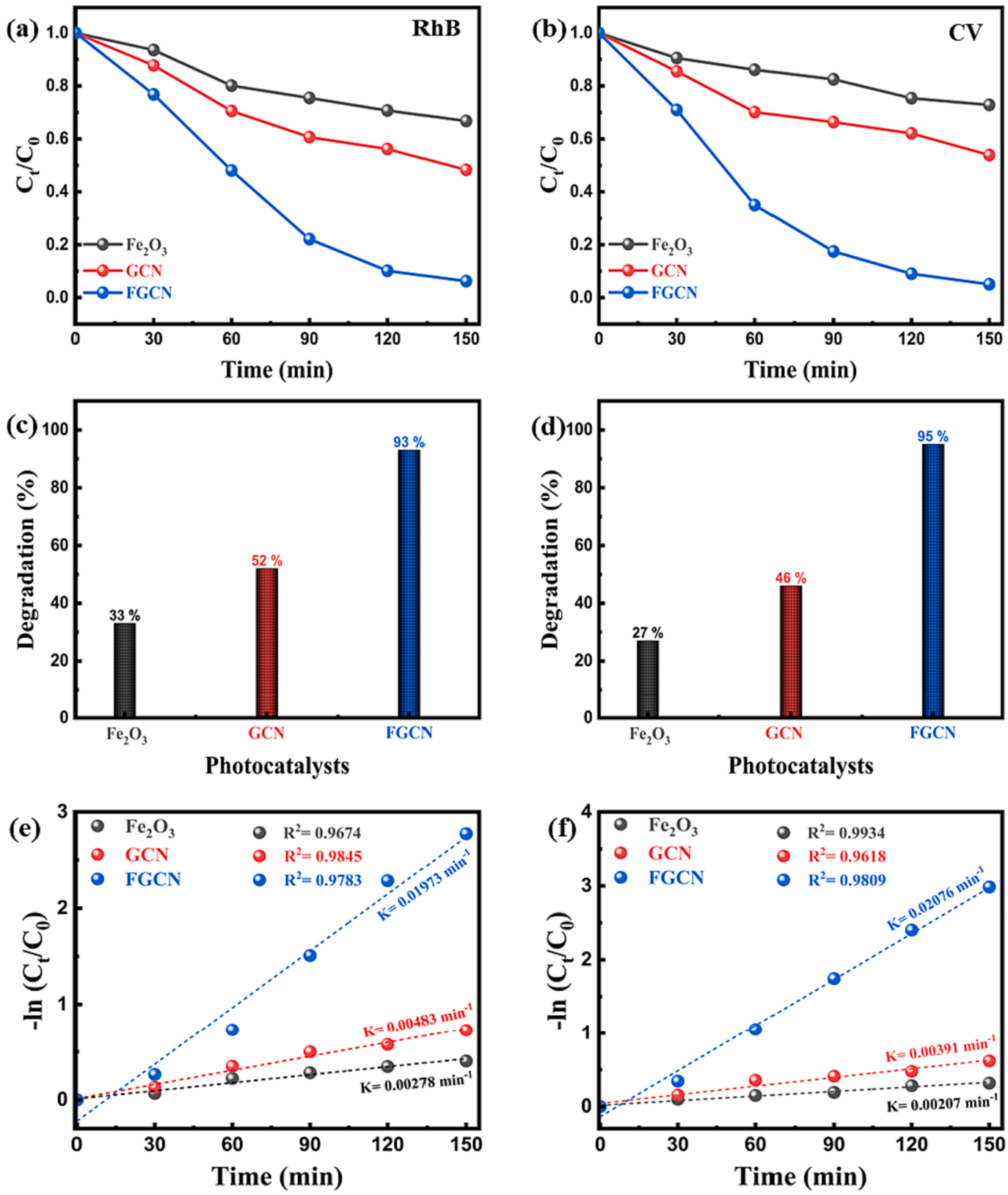

Fig.7. Photo-degradation performance of (a) RhB, (b) CV, (c, d) degradation efficiency of RhB and CV at 150 min, and (e, f) corresponding kinetic curves of as-fabricated materials under solar light irradiation.

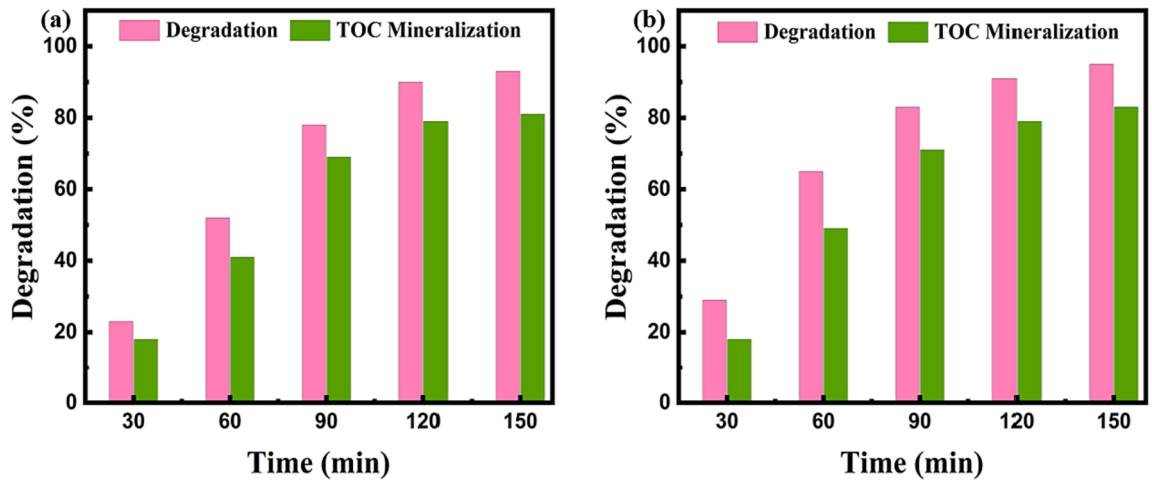

Fig. 8. TOC analysis of (a) RhB and (b) CV solution during photodegradation.

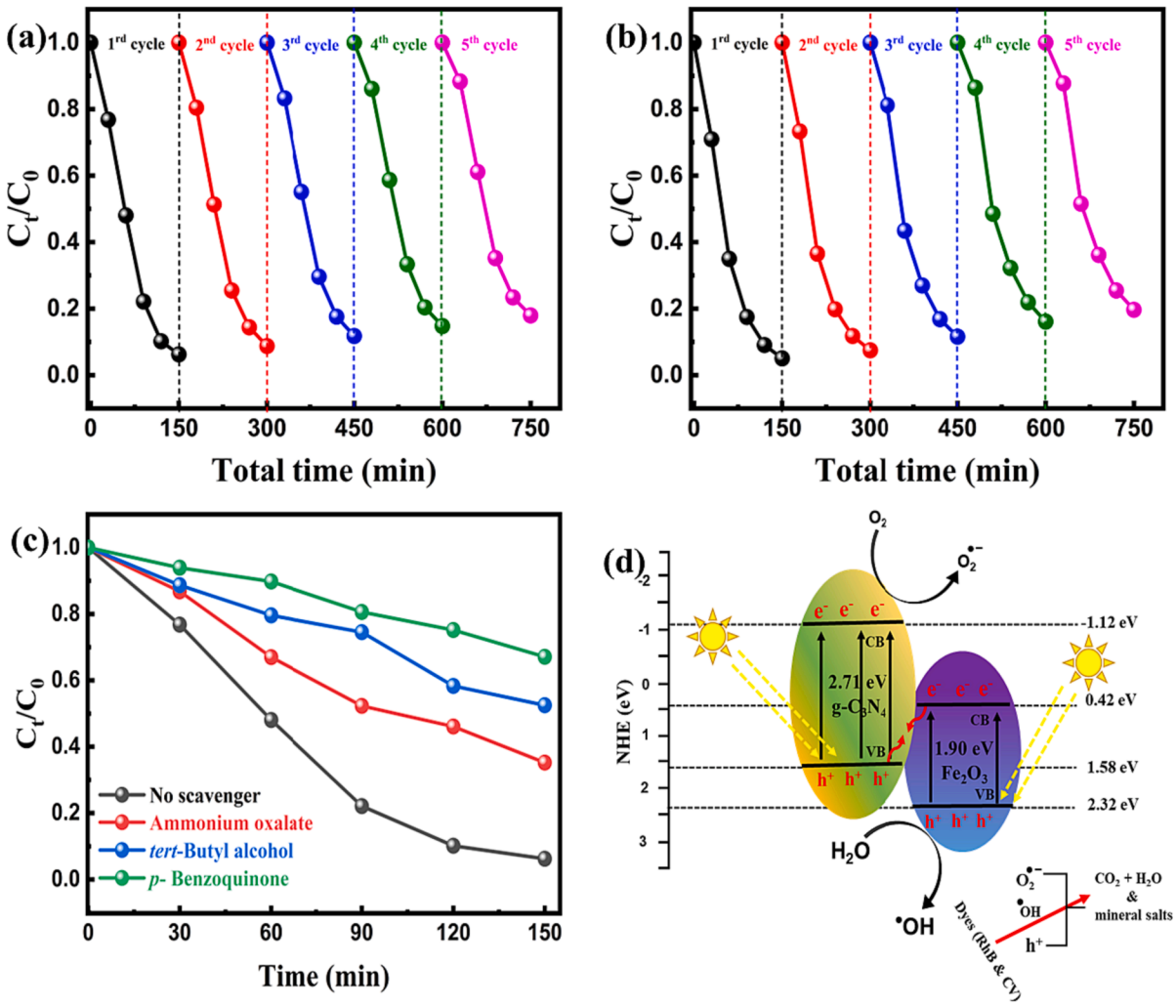

Fig. 9. (a, b) Reusability test of RhB and CV dyes, (c) Scavenging test for RhB, and (d) Possible photocatalytic degradation mechanism of FGCN composite catalyst.

potentials (CB of Fe_2O_3 and VB of GCN) are not feasible for the formations of ROS such as superoxide radical anions ($O_2^{\bullet-}$) and hydroxyl radicals ($^{\bullet}OH$), since CB of Fe_2O_3 is less negative when compared with standard redox potential of $O_2^{\bullet-}$ ($O_2/O_2^{\bullet-} = -0.33$ eV vs NHE) [63], and also the VB of GCN is less positive when compared with standard redox potential of $^{\bullet}OH$ ($^{-}OH/^{\bullet}OH = +1.99$ eV vs. NHE) [63]. At this condition, it has been proposed that the recombination of e^- and h^+ ions effectively prevents the recombination of the corresponding e^-/h^+ pair through the formation of Z-scheme heterojunction through the coupling of GCN and Fe_2O_3 [64,65]. In the composite Z-scheme heterojunction

system, the excited electrons in the CB of Fe_2O_3 can easily transfer to the VB of GCN. This transfer allows direct reformation of GCN by h^+ in the VB. The CB potential electron of GCN is negative enough to react with the O_2 adsorbed on the FGCN surface. This reaction generates a redox potential of $O_2^{\bullet-}$ ($O_2/O_2^{\bullet-} = -0.33$ eV vs NHE). At the same time, the h^+ present in the VB of Fe_2O_3 has significantly improved oxidation ability and is thermodynamically favorable (VB = +2.32 eV) for the formation of $^{\bullet}OH$. This advantage is particularly evident in the case of dye decomposition processes, where the $^{-}OH/^{\bullet}OH$ potential is + 1.99 eV vs NHE. Therefore, RhB and CV dyes can be oxidized to H_2O and CO_2 or other by-products [66]. The following equation describes the reactions involved in the photocatalytic process of organic dye decomposition and electron-hole pair formation within the FGCN composite:

$$FGCN + h\nu \rightarrow (FGCN)_{CB}\ e^- + (FGCN)_{VB}\ h^+ \quad (3)$$

$$O_2 + (FGCN)_{CB}\ e^- \rightarrow O_2^{\bullet-} \quad (4)$$

$$h^+ + {}^{-}OH \rightarrow {}^{\bullet}OH \quad (5)$$

$$(O_2^{\bullet-} + {}^{\bullet}OH) + \text{RhB and CV dye} \rightarrow CO_2 + H_2O \quad (6)$$

3.3. Electrochemical performance

The electrochemical oxygen evolution reaction (OER) performance of GCN@NF, Fe_2O_3@NF, FGCN@NF, and IrO_2@NF electrodes were evaluated using an electrochemical system with a scan rate of 5 mV/s in 1 M KOH electrolyte solution. Fig. 10a shows the linear sweep voltammetry (LSV) profiles of GCN@NF, Fe_2O_3@NF, FGCN@NF, and IrO_2@NF heterostructure composites. These curves show that the potential values for the RHE at a current density of 10 mA/cm^2 are 1.62 V, 1.54 V, 1.52 V, and 1.45 V, respectively. The FGCN@NF catalyst sample showed superior OER activity at lower potential values compared to the Fe_2O_3@NF and GCN@NF samples. The improved OER performance of FGCN@NF

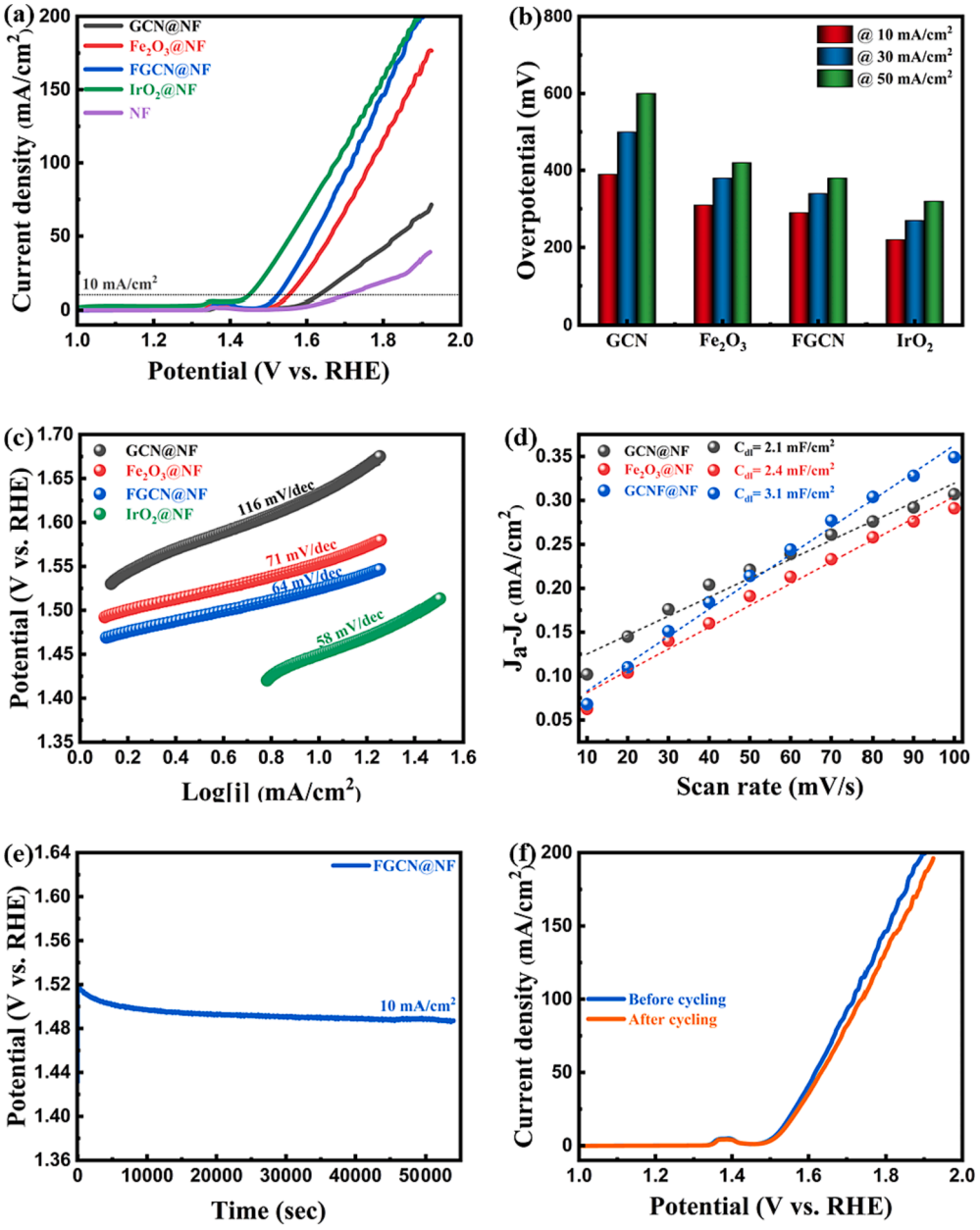

Fig. 10. (a) LSV curve, (b) measured overpotential values at the different current densities. (c) Tafel slopes, (d) determined double-layer capacitance (C_{dl}), (e) chronopotentiometry curves for 15 h at 10 mA/cm ^{2} and (f) LSV measured before and after the stability test.

heterostructure composites can be attributed to the strengthened bonding at the interface of GCN and Fe_2O_3 and the increased number of active sites. Therefore, this composite heterostructure has the potential to achieve performance levels similar to conventional IrO_2 catalysts. Fig. 10b shows that the FGCN@NF has a lower overpotential (290 mV at 10 mA/cm^2) when compared to the Fe_2O_3@NF and GCN@NF electrodes with overpotentials of 310, and 390 mV at 10 mA/cm^2, respectively. This indicates an improvement in the efficiency of OER by the combination of GCN with Fe_2O_3. Furthermore, the electron transfer process in the reaction system results in a synergistic coupling effect, resulting in a decrease in the Gibbs free energy associated with proton absorption and desorption [67,68]. This energy reduction improves the overall performance of OER. The lower Tafel plot suggests a rapid increase in current density, indicating enhanced electrochemical water splitting and faster OER kinetics.

Fig. 10c shows the Tafel slopes of the oxygen evolution reaction using GCN@NF, Fe_2O_3@NF, FGCN@NF, and IrO_2@NF electrodes were 116, 71, 64, and 58 mV/dec, respectively. Particularly, the FGCN@NF electrocatalyst exhibited the lowest Tafel slope compared to synthesized materials, due to the synergistic effect of the composite. As a result, the FGCN@NF composite effectively improved the electrocatalytic performance and reaction kinetics of OER. Fig. S5 shows the CV curves and Fig. 10d shows the C_{dl} value of Fe_2O_3@NF, GCN@NF, and FGCN@NF. The calculated C_{dl} (double-layer capacitance) of the FGCN@NF composite catalyst reaches 3.1 mF/cm^2, which is higher than that of Fe_2O_3@NF (2.4 mF/cm^2) and (2.1 mF/cm^2) GCN@NF. This improvement in OER catalytic activity in the FGCN@NF composite catalyst is attributed not only to the increase in electrochemically active surface area (ECSA) but also to the optimal chemisorption energy of the active sites. The low charge transfer resistance at the heterostructure interface and the significant interfacial electronic coupling effect of Fe_2O_3 on the active GCN nanosheets contribute to the improved performance [69]. This study included an investigation on the long-term stability of the performance of FGCN@NF composite catalyst in OER reaction. Table S3 shows the ECSA, surface activity, and TOF values of the prepared electrocatalysts. The FGCN composite catalyst exhibited high TOF compared to other synthesized catalysts, further confirming its superior performance in electrochemical OER reactions. The enhanced OER catalytic activity of the FGCN composite catalysts can be attributed not only to the increased ECSA value but also to the combination of low charge transfer resistance and strong interfacial electronic coupling effect between Fe_2O_3 and GCN nanostructures.

In Fig. 10e, a chronopotentiometry investigation was achieved at a current density of 10 mA/cm ^{2}, revealing the remarkable electrocatalytic efficiency of the material. It maintained its effectiveness even after undergoing extensive testing for 54,000 s. In particular, the sustained performance of the catalyst over long periods of continuous OER conditions is an important factor for its potential practical application. The LSV curves for the initial LSV curve and after the LSV curve of the FGCN@NF composite are shown in Fig. 10f. Remarkably, even after a 15 h LSV curve at a constant current density of 10 mA/cm^2, the overpotential showed no significant change of 10 mA/cm^2. This result highlights the remarkable long-lasting effect of the FGCN@NF composite heterostructure in terms of efficient OER activity. Table S4 presents a comparative analysis of the electrochemical performance of Fe-based electrocatalysts, contrasting previously established ones with recently introduced ones.

Effective OER electrocatalytic activity in a two-electrode system for as-synthesized Pt/C@NF||IrO_2@NF and Pt/C@NF||FGCN@NF to evaluate their potential applications using 1 M KOH and corresponding results are shown in Fig. 11. The illustrated in Fig. 11, also includes an evaluation of the catalytic performance of the commercial Pt/C@NF||IrO_2@NF couple for reference. Notably, the Pt/C@NF||FGCN@NF sample demonstrated the ability to achieve a current density of 10 mA/cm^2 at a cell voltage of approximately 1.61 V, and which is comparable with Pt/C@NF||IrO_2@NF electrode (1.52 V). The improved water splitting efficiency was evident by the significant release of O_2 bubbles during electrolysis, which contributed to the improved commercial feasibility [70,71]. Additionally, a chronopotentiometry test was performed at a current density of 10 mA/cm^2 to evaluate the durability of the electrocatalyst. The corresponding results shown in Fig. 11b clearly show that Pt/C@NF||FGCN@NF exhibits excellent long-term stability over 15 h and demonstrates good corrosion resistance against alkaline electrolytes. These findings are consistent with good performance in OER. Table S5 provides additional comparisons of recently reported catalysts by two-electrode analysis.

4. Conclusion

In summary, we successfully synthesized GCN, Fe_2O_3, and FGCN composite catalysts using thermal polymerization and hydrothermal techniques. HR-TEM examination specifically confirmed the presence of a mixture of GCN and Fe_2O_3 in the FGCN composite. The FGCN composite catalyst demonstrated excellent photocatalytic degradation efficiency in the removal of RhB (93 %) and CV (95 %) aqueous dyes under 150 min of sunlight exposure. Remarkably, the rate constants (k) of RhB and CV dye decomposition on FGCN composite catalyst are 0.01973 min^{-1} and 0.02076 min^{-1}, which is about 7.0 & 4.0 and 10.0 & 5.3 folds superior to those of Fe_2O_3 and GCN photocatalyst, respectively. Furthermore, the FGCN composite catalyst showed excellent recyclability even after five consecutive cycles. Besides, the trapping test reveals that the main active species during the photodegradation process

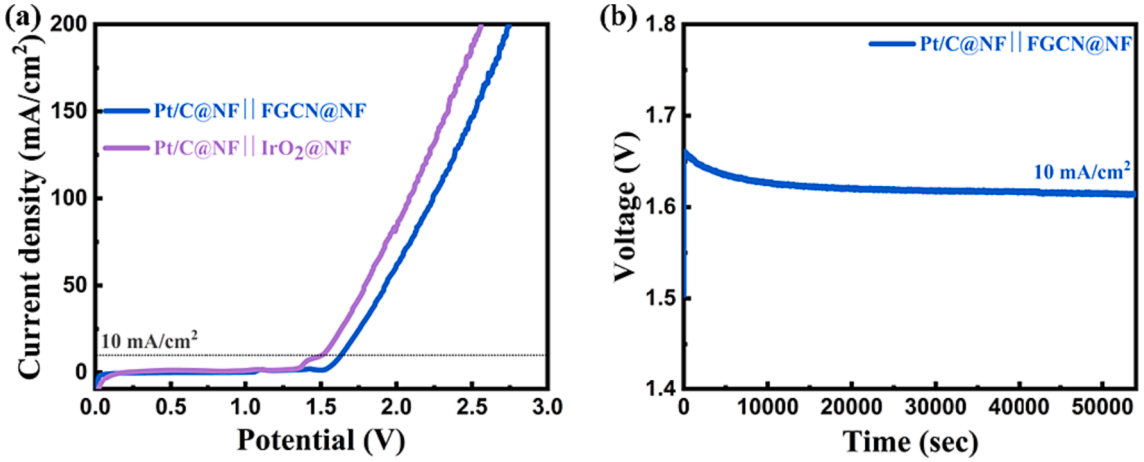

Fig. 11. Electrochemical measurements in the two-electrode system (a) LSV curves and (b) Stability test for 15 h at 10 mA/cm^2 of the FGCN@NF electrocatalyst.

were $O_2^{\bullet-}$ and $^{\bullet}OH$. The combination of GCN with Fe_2O_3@NF improved the OER efficiency. The synergistic coupling effect of electron transfer reduced the Gibbs free energy of proton absorption and desorption, thereby enhancing the OER activity. The Tafel slopes of GCN@NF, Fe_2O_3@NF, and FGCN@NF electrodes in the OER reaction were 116, 71, 64, and 58 mV/dec, respectively. The synthesized composite was proven to be effective in degrading RhB and CV dyes under direct sunlight and showed enhanced photo/electrocatalytic activities.

CRediT authorship contribution statement

Sakthivel Kumaravel: Writing – original draft, Methodology, Formal analysis, Conceptualization. **Balakrishna Avula:** Formal analysis, Software. **Chandramoorthy Chandrasatheesh:** Methodology, Formal analysis, Data curation. **Theophile Niyitanga:** Software, Validation. **Rajasekar Saranya:** Resources, Formal analysis. **Imran Hasan:** Software, Formal analysis, Data curation. **T. Abisheik:** Formal analysis, Software. **Rajakumar S. Rai:** Validation. **V. Pandiyan:** Writing – review & editing. **Krishnakumar Balu:** Writing – review & editing, Supervision, Conceptualization.

Declaration of Competing Interest

The authors declare that they have no known competing financial interests or personal relationships that could have appeared to influence the work reported in this paper.

Data availability

Data will be made available on request.

Acknowledgments

The authors extend their thanks to Researchers Supporting Project (Ref: RSPD2024R670), King Saud University, Riyadh, Saudi Arabia. Dr. Krishnakumar Balu would like to thank the Ministry of Universities and the Recovery, Transformation, and Resilience Plan from the Spanish government for the "María Zambrano Grant 2021" by the European Union – NextGenerationEU.

Appendix A. Supplementary material

Fig. S1 XRD patterns of the as-synthesized MOF-Fe_2O_3 sample before calcination. Fig. S2 Absorption evolution spectra of RhB and CV dyes for the most active FGCN composite catalyst. Fig. S3. XRD analysis of fresh and spend most active FGCN composite catalyst. Fig. S4 FE-SEM images and elemental mapping and EDS image of used FGCN composite catalyst. Fig. S5. CV measured in non-faradaic regions at different scan rates of the prepared sample. Table S1. Different dye degradation and rate constant using FGCN composite catalyst at 150 min. Table S2. Comparison of photocatalytic performance by various Fe-based catalysts. Table S3. OER performance of as-prepared materials. Table S4. Comparison of OER performance by various Fe-based electrocatalysts. Table S5. Comparison of two electrode OER performance by various Fe-based electrocatalysts. Supplementary data to this article can be found online at https://doi.org/10.1016/j.saa.2024.123972.

References

[1] K.G. Pavithra, S.K. P., V. Jaikumar, S.R. P., Removal of colorants from wastewater: a review on sources and treatment strategies, J. Ind. Eng. Chem. 75 (2019) 1–19. 10.1016/J.JIEC.2019.02.011.
[2] E. Brillas, C.A. Martínez-Huitle, Decontamination of wastewaters containing synthetic organic dyes by electrochemical methods. An updated review, Appl. Catal. B Environ. 166–167 (2015) 603–643, https://doi.org/10.1016/J.APCATB.2014.11.016.
[3] R. Al-Tohamy, S.S. Ali, F. Li, K.M. Okasha, Y.A.G. Mahmoud, T. Elsamahy, H. Jiao, Y. Fu, J. Sun, A critical review on the treatment of dye-containing wastewater: Ecotoxicological and health concerns of textile dyes and possible remediation approaches for environmental safety, Ecotoxicol. Environ. Saf. 231 (2022) 113160, https://doi.org/10.1016/J.ECOENV.2021.113160.
[4] H. Cao, R. Wang, K. Dou, J. Qiu, C. Peng, N. Tsidaeva, W. Wang, High-efficiency adsorption removal of CR and MG dyes using AlOOH fibers embedded with porous $CoFe_2O_4$ nanoparticles, Environ. Res. 216 (2023) 114730, https://doi.org/10.1016/J.ENVRES.2022.114730.
[5] S. Kumaravel, S. Thiripuranthagan, T. Vembuli, E. Erusappan, M. Durai, T. Sureshkumar, M. Durai, Fabrication of mesoporous WO_3-SBA-15 catalysts and enhanced photocatalytic degradation of harmful dyes, Optik (stuttg). 235 (2021) 166599, https://doi.org/10.1016/j.ijleo.2021.166599.
[6] R. Kishor, D. Purchase, G.D. Saratale, R.G. Saratale, L.F.R. Ferreira, M. Bilal, R. Chandra, R.N. Bharagava, Ecotoxicological and health concerns of persistent coloring pollutants of textile industry wastewater and treatment approaches for environmental safety, J. Environ. Chem. Eng. 9 (2021) 105012, https://doi.org/10.1016/J.JECE.2020.105012.
[7] J. Xu, J. Shen, H. Jiang, X. Yu, W. Ahmad Qureshi, C. Maouche, J. Gao, J. Yang, Q. Liu, Progress and challenges in full spectrum photocatalysts: Mechanism and photocatalytic applications, J. Ind. Eng. Chem. 119 (2023) 112–129, https://doi.org/10.1016/J.JIEC.2022.11.057.
[8] M. Pavel, C. Anastasescu, R.N. State, A. Vasile, F. Papa, I. Balint, Photocatalytic degradation of organic and inorganic pollutants to harmless end products: assessment of practical application potential for water and air cleaning, Catal. 2023, Vol. 13, Page 380. 13 (2023) 380. 10.3390/CATAL13020380.
[9] P.J. Megia, A.J. Vizcaino, J.A. Calles, A. Carrero, Hydrogen production technologies: from fossil fuels toward renewable sources. A mini review, Energy Fuels 35 (2021) 16403–16415, https://doi.org/10.1021/ACS.ENERGYFUELS.1C02501/ASSET/IMAGES/LARGE/EF1C02501_0004.JPEG.
[10] G.K. Gebremariam, A.Z. Jovanovićjovanović, I.A. Pašti, The effect of electrolytes on the kinetics of the hydrogen evolution reaction, Hydrogen 4 (2023) 776–806, https://doi.org/10.3390/HYDROGEN4040049.
[11] Y. Li, X. Jiang, M. Tang, Q. Zheng, Y. Huo, F. Xie, D. Lin, A high-performance oxygen evolution electrocatalyst based on partially amorphous bimetallic cobalt iron boride nanosheet, Int. J. Hydrogen Energy. 45 (2020) 28586–28597, https://doi.org/10.1016/J.IJHYDENE.2020.07.140.
[12] F. Song, L. Bai, A. Moysiadou, S. Lee, C. Hu, L. Liardet, X. Hu, Transition metal oxides as electrocatalysts for the oxygen evolution reaction in alkaline solutions: an application-inspired renaissance, J. Am. Chem. Soc. 140 (2018) 7748–7759, https://doi.org/10.1021/JACS.8B04546/ASSET/IMAGES/MEDIUM/JA-2018-04546Q_0007.GIF.
[13] S. Balgude, S. Godase, A. Shinde, C. Harak, Succinate assisted synthesis of magnetically separable Fe_2O_3/g-C_3N_4 nano-heterostructure: a stable catalyst for environmental remediation, Curr. Res. Green Sustain. Chem. 4 (2021) 100210, https://doi.org/10.1016/J.CRGSC.2021.100210.
[14] A.B. Baral, B. Dash, M.K. Ghosh, T. Subbaiah, M. Minakshi, Pathway of sucrose oxidation in manganese (pyrolusite) nodule, Ind. Eng. Chem. Res. 54 (2015) 12233–12241, https://doi.org/10.1021/acs.iecr.5b02881.
[15] M. Minakshi, Examining manganese dioxide electrode in KOH electrolyte using TEM technique, J. Electroanal. Chem. 616 (2008) 99–106, https://doi.org/10.1016/j.jelechem.2008.01.011.
[16] X. Lu, S. Tang, W. Chen, J. Xu, Y. Zeng, X. Wang, X. Peng, J. Li, B. Hong, Exploring the enhancement of exchange bias in α-Fe_2O_3/g-C_3N_4 composites: Synthesis, magnetic properties and a first-order reversal curve analysis, J. Alloys Compd. 969 (2023) 172308, https://doi.org/10.1016/J.JALLCOM.2023.172308.
[17] D. Meng, J. Hou, L. Wang, X. Hu, D. Gao, Q. Guo, Rational construction of α-Fe_2O_3/g-C_3N_4 heterojunction for effective photo-Fenton-like degradation of tetracycline, Mater. Res. Bull. 168 (2023) 112454, https://doi.org/10.1016/J.MATERRESBULL.2023.112454.
[18] Y. Geng, D. Chen, N. Li, Q. Xu, H. Li, J. He, J. Lu, Z-Scheme 2D/2D α-Fe_2O_3/g-C_3N_4 heterojunction for photocatalytic oxidation of nitric oxide, Appl. Catal. B Environ. 280 (2021) 119409, https://doi.org/10.1016/J.APCATB.2020.119409.
[19] X. Zhou, H. Liu, S. Liu, L. zhang, T. Wang, C. Wang, D. Su, Constructing efficient α-Fe_2O_3/g-C_3N_4/HNTs-loaded heterojunction photocatalysts for photocatalytic oxidative desulfurization: Influencing factors, kinetics, and mechanism, Fuel. 332 (2023) 126147. 10.1016/J.FUEL.2022.126147.
[20] M.J. Molaei, Graphitic carbon nitride (g-C3N4) synthesis and heterostructures, principles, mechanisms, and recent advances: a critical review, Int. J. Hydrogen Energy. 48 (2023) 32708–32728, https://doi.org/10.1016/J.IJHYDENE.2023.05.066.
[21] J.A.S. Syed, X.Y. Zhang, W.J. Ding, A.D. Li, An overview of the current progress of graphitic carbon nitride and its multifunctional applications, J. Environ. Chem. Eng. 10 (2022) 108745, https://doi.org/10.1016/J.JECE.2022.108745.
[22] J. Wen, J. Xie, X. Chen, X. Li, A review on g-C_3N_4-based photocatalysts, Appl. Surf. Sci. 391 (2017) 72–123, https://doi.org/10.1016/J.APSUSC.2016.07.030.
[23] S. Iqbal, J. Liu, H. Ma, W. Liu, S. Zuo, Y. Yu, Fabrication of TiO_2/Fe_2O_3/g-C_3N_4 ternary photocatalyst via a low-temperature calcination and solvothermal route and its visible light assisted photocatalytic properties, J. Mol. Struct. 1282 (2023) 135166, https://doi.org/10.1016/J.MOLSTRUC.2023.135166.
[24] M. Danish, M. Saud Athar, I. Ahmad, M.Z.A. Warshagha, Z. Rasool, M. Muneer, Highly efficient and stable Fe_2O_3/g-C_3N_4/GO nanocomposite with Z-scheme electron transfer pathway: Role of photocatalytic activity and adsorption isotherm of organic pollutants in wastewater, Appl. Surf. Sci. 604 (2022) 154604, https://doi.org/10.1016/J.APSUSC.2022.154604.
[25] C. Yavuz, S. Erten-Ela, Solar light-responsive α-Fe_2O_3/CdS/g-C_3N_4 ternary photocatalyst for photocatalytic hydrogen production and photodegradation of

methylene blue, J. Alloys Compd. 908 (2022) 164584, https://doi.org/10.1016/J.JALLCOM.2022.164584.
[26] C. Thambiliyagodage, A. Kumara, M. Jayanetti, L. Usgodaarachchi, H. Liyanaarachchi, B. Lansakara, Fabrication of dual Z-scheme g-C_3N_4/Fe_2TiO_5/Fe_2O_3 ternary nanocomposite using natural ilmenite for efficient photocatalysis and photosterilization under visible light, Appl. Surf. Sci. Adv. 12 (2022) 100337, https://doi.org/10.1016/J.APSADV.2022.100337.
[27] U.Q. Satti, S.J.A. Zaidi, A. Riaz, M.A. ur Rehman, C.X. Li, M.A. Basit, Simple two-step development of TiO_2/Fe_2O_3 nanocomposite for oxygen evolution reaction (OER) and photo-bio active applications, Colloids Surfaces A Physicochem. Eng. Asp. 671 (2023) 131662. 10.1016/J.COLSURFA.2023.131662.
[28] H. Mosallaei, H. Hadadzadeh, A.A. Ensafi, K.Z. Mousaabadi, M. Weil, A. Foelske, M. Sauer, Evaluation of HER and OER electrocatalytic activity over RuO_2–Fe_2O_3 nanocomposite deposited on HrGO nanosheets, Int. J. Hydrogen Energy. 48 (2023) 1813–1830, https://doi.org/10.1016/J.IJHYDENE.2022.10.026.
[29] I. Ahmad, J. Ahmed, S. Batool, M.N. Zafar, A. Hanif, M.F. Zahidullah, A. Nazar, U. Ul-Hamid, A. Jabeen, M. Dahshan, S.A.S. Idrees, Design and fabrication of Fe_2O_3/FeP heterostructure for oxygen evolution reaction electrocatalysis, J. Alloys Compd. 894 (2022) 162409, https://doi.org/10.1016/J.JALLCOM.2021.162409.
[30] B. Shabbir, M.Z. Ansari, S. Manzoor, A.G. Abid, M.U. Nisa, A.M. Shawky, S. Znaidia, S. Aman, M.N. Ashiq, T.A. Taha, Facile synthesis of Er-MOF/Fe_2O_3 nanocomposite for oxygen evolution reaction, Mater. Chem. Phys. 292 (2022) 126861, https://doi.org/10.1016/J.MATCHEMPHYS.2022.126861.
[31] R.R. Palem, A. Meena, R. Soni, J. Meena, S.H. Lee, S.A. Patil, S. Ansar, H.S. Kim, H. Im, C. Bathula, Fabrication of Fe_2O_3 nanostructure on CNT for oxygen evolution reaction, Ceram. Int. 48 (2022) 29081–29086, https://doi.org/10.1016/J.CERAMINT.2022.04.322.
[32] S.S. Kumaravel, M. Durai, R. Sepúlveda, E. Chicardi, S.S. Kumaravel, M.J. Kim, K. Balu, I. Hasan, K. Srinivasan, Y.H. Ahn, Fabrication of Ag/WO_3/g-C_3N_4 composites for the photocatalytic degradation of harmful dyes, Opt. Mater. (amst). 144 (2023) 114322, https://doi.org/10.1016/j.optmat.2023.114322.
[33] S. Kumaravel, C. Chandrasatheesh, G. Palanisamy, J. Lee, I. Hasan, S. Kumaravel, B. Avula, U.D. Pongiya, K. Balu, Highly efficient solar-light-active Ag-decorated g-C_3N_4 composite photocatalysts for the degradation of methyl orange dye, Micromachines. 14 (2023) 1454, https://doi.org/10.3390/mi14071454.
[34] C. Tang, M. Cheng, C. Lai, L. Li, Z. Wei, D. Ma, L. Du, G. Wang, L. Yang, L. Tang, Multiple path-dominated activation of peroxymonosulfate by MOF-derived Fe_2O_3/Mn_3O_4 for catalytic degradation of tetracycline, J. Environ. Chem. Eng. 11 (2023) 110395, https://doi.org/10.1016/J.JECE.2023.110395.
[35] E. Rojas García, G. Pérez-Soreque, R. López Medina, F. Rubio-Marcos, A. M. Maubert-Franco, CNTs/Fe-BTC composite materials for the CO_2-photocatalytic reduction to clean fuels: batch and continuous system, Molecules. 28 (2023) 4738, https://doi.org/10.3390/molecules28124738.
[36] M. Roostaee, H. Beitollahi, I. Sheikhshoaie, Simultaneous determination of dopamine and uric acid in real samples using a voltammetric nanosensor based on Co-MOF, graphene oxide, and 1-methyl-3-butylimidazolium bromide, Micromachines. 13 (2022) 1834, https://doi.org/10.3390/mi13111834.
[37] N. Riezzati, Y.K. Krisnandi, A. Zulys, Metal organic frameworks of lanthanum and iron using BDC linker as catalysts for glucose conversion into 5-hydroxymethyl-furfural (5-HMF), IOP Conf. Ser. Mater. Sci. Eng. 902 (2020) 012044, https://doi.org/10.1088/1757-899X/902/1/012044.
[38] X. Ling, F. Du, Y. Zhang, Y. Shen, T. Li, A. Alsaedi, T. Hayat, Y. Zhou, Z. Zou, Preparation of an Fe_2Ni MOF on nickel foam as an efficient and stable electrocatalyst for the oxygen evolution reaction, RSC Adv. 9 (2019) 33558–33562, https://doi.org/10.1039/C9RA07499F.
[39] M. Durai, Y.H. Ahn, Photocatalytic H_2 generation under blue and white LEDs by Fe_2O_3 /KTLO/rGO S-scheme composite photocatalyst, J. Alloys Compd. 965 (2023) 171457, https://doi.org/10.1016/J.JALLCOM.2023.171457.
[40] Y. Zhan, L. Shen, C. Xu, W. Zhao, Y. Cao, L. Jiang, MOF-derived porous Fe_2O_3 with controllable shapes and improved catalytic activities in H_2S selective oxidation, CrystEngComm. 20 (2018) 3449–3454, https://doi.org/10.1039/C8CE00552D.
[41] T. Sureshkumar, S. Thiripuranthagan, S.M.K. Paskalis, S. Kumaravel, K. Kannan, A. Devarajan, Synthesis, characterization and photodegradation activity of graphitic C_3N_4-$SrTiO_3$ nanocomposites, J. Photochem. Photobiol. A Chem. 356 (2018) 425–439, https://doi.org/10.1016/J.JPHOTOCHEM.2018.01.027.
[42] S. Kumaravel, H. Kim, Development and characterization of solar active Ag-ZnO/g-C_3N_4 as a highly efficient photocatalyst for the detoxification of organic pollutant, Colloids Surfaces A Physicochem. Eng. Asp. 679 (2023) 132644, https://doi.org/10.1016/j.colsurfa.2023.132644.
[43] Z. Masoumi, M. Tayebi, M. Kolaei, B.K. Lee, Improvement of surface light absorption of ZnO photoanode using a double heterojunction with α–Fe_2O_3/g–C_3N_4 composite to enhance photoelectrochemical water splitting, Appl. Surf. Sci. 608 (2023) 154915, https://doi.org/10.1016/J.APSUSC.2022.154915.
[44] R. Parvari, F. Ghorbani-Shahna, A. Bahrami, S. Azizian, M.J. Assari, M. Farhadian, A novel core-shell structured α-Fe_2O_3/Cu/g-C_3N_4 nanocomposite for continuous photocatalytic removal of air ethylbenzene under visible light irradiation, J. Photochem. Photobiol. A Chem. 399 (2020) 112643, https://doi.org/10.1016/J.JPHOTOCHEM.2020.112643.
[45] S. Kumaravel, J.K. Alagarasan, A.K. Yadav, W. Ali, M. Lee, M.E. Khan, S.K. Ali, A. H. Bashiri, W. Zakri, K. Balu, Highly selective catalytic transfer hydrogenation of biomass derived furfural to furfural alcohol over Zr/SBA-15 catalysts, J. Phys. Chem. Solids. 186 (2024) 111831, https://doi.org/10.1016/j.jpcs.2023.111831.
[46] N. Mao, Investigating the Heteronjunction between ZnO/Fe_2O_3 and g-C_3N_4 for an Enhanced Photocatalytic H2 production under visible-light irradiation, Sci. Reports 2019 91. 9 (2019) 1–9. 10.1038/s41598-019-48730-z.
[47] Q. Xu, B. Zhu, C. Jiang, B. Cheng, J. Yu, Constructing 2D/2D Fe_2O_3/g-C_3N_4 direct Z-scheme photocatalysts with enhanced H_2 generation performance, Sol. RRL. 2 (2018) 1800006, https://doi.org/10.1002/SOLR.201800006.
[48] B. Es, Photocatalytic removal of Pb ions from aqueous solution using Fe_2O_3 doped in G-C_3N_4 nanocomposite under visible light, Front. Nanosci. Nanotechnol. Res. 2 (2016) 100–106, https://doi.org/10.15761/FNN.1000116.
[49] K. Sharma, A. Sudhaik, P. Raizada, P. Thakur, X.M. Pham, Q. Van Le, V.H. Nguyen, T. Ahamad, S. Thakur, P. Singh, Constructing α-Fe_2O_3/g-C_3N_4/SiO_2 S-scheme-based heterostructure for photo-Fenton like degradation of rhodamine B dye in aqueous solution, Environ. Sci. Pollut. Res. (2023) 1–19, https://doi.org/10.1007/S11356-022-24940-3/METRICS.
[50] D. Sun, L. Jia, C. Wang, H. Liu, R. Chen, Preparation of the additive-modified α-Fe_2O_3/g-C_3N_4 Z-scheme composites with improved visible-light photocatalytic activity, J. Environ. Chem. Eng. 9 (2021) 106274, https://doi.org/10.1016/J.JECE.2021.106274.
[51] T.P. Vijayakumar, M.D. Benoy, J. Duraimurugan, G.S. Kumar, M. Shkir, P. Maadeswaran, R. Srinivasan, S. Prabhu, R. Ramesh, S. Haseena, Investigation on photocatalytic activity of g-C_3N_4 decorated α-Fe_2O_3 nanostructure synthesized by hydrothermal method for the visible-light assisted degradation of organic pollutant, Diam. Relat. Mater. 125 (2022) 109021, https://doi.org/10.1016/J.DIAMOND.2022.109021.
[52] S.H. Park, T. Kim, A.N. Kadam, C. Bathula, A.A. Ghfar, H. Kim, S.W. Lee, Synergistic photocatalysis of Z-scheme type Fe_2O_3/g-C_3N_4 heterojunction coupled with reduced graphene oxide, Surfaces Interfaces 30 (2022) 101910, https://doi.org/10.1016/J.SURFIN.2022.101910.
[53] G. Mummoorthi, S. Arjunan, M. Selvaraj, S.L. Rokhum, N. Mani, S. Periyasamy, R. Rajendran, High-performance solid-state asymmetric Supercapacitor based on α-Fe_2O_3/r-GO/GCN composite electrode material for energy storage application, Surfaces Interfaces. 41 (2023) 103166, https://doi.org/10.1016/J.SURFIN.2023.103166.
[54] W. Cheng, J. He, T. Yao, Z. Sun, Y. Jiang, Q. Liu, S. Jiang, F. Hu, Z. Xie, B. He, W. Yan, S. Wei, Half-unit-cell α-Fe_2O_3 semiconductor nanosheets with intrinsic and robust ferromagnetism, J. Am. Chem. Soc. 136 (2014) 10393–10398, https://doi.org/10.1021/JA504088N/SUPPL_FILE/JA504088N_SI_001.PDF.
[55] F. Qiao, J. Wang, S. Ai, L. Li, As a new peroxidase mimetics: the synthesis of selenium doped graphitic carbon nitride nanosheets and applications on colorimetric detection of H_2O_2 and xanthine, Sens. Actuat. B Chem. 216 (2015) 418–427, https://doi.org/10.1016/J.SNB.2015.04.074.
[56] P. Govindasamy, B. Kandasamy, P. Thangavelu, S. Barathi, M. Thandavarayan, M. Shkir, J. Lee, Biowaste derived hydroxyapatite embedded on two-dimensional g-C_3N_4 nanosheets for degradation of hazardous dye and pharmacological drug via Z-scheme charge transfer, Sci. Rep. 12 (2022) 11572, https://doi.org/10.1038/s41598-022-15799-y.
[57] L. Shen, Z. Xing, J. Zou, Z. Li, X. Wu, Y. Zhang, Q. Zhu, S. Yang, W. Zhou, Black TiO_2 nanobelts/g-C_3N_4 nanosheets Laminated Heterojunctions with Efficient Visible-Light-Driven Photocatalytic Performance, Sci. Reports 2017 71. 7 (2017) 1–11. 10.1038/srep41978.
[58] K. Balu, S. Ramasundaram, R. Sepúlveda, E. Chicardi, S. Kumaravel, J. Josphin Mini, T. Hwan Oh, B. Avula, A.J.F.N. Sobral, Synthesis and characterization of visible active Fe grafted ZnO nanocomposites for NBB degradation in water, Inorg. Chem. Commun. 154 (2023) 110963, https://doi.org/10.1016/j.inoche.2023.110963.
[59] D. Mani, D. Mathivanan, H. Chang, K. Sakthivel, E. Elangovan, T. Sivakumar, M. Arivanandhan, R. Jayavel, A facile synthesis of novel ε-Fe_2O_3 grafted 2D h-BN nanostructures for enhanced visible active photocatalytic applications, New J. Chem. 44 (2020) 12289–12298, https://doi.org/10.1039/D0NJ02321C.
[60] S. Kumaravel, S. Thiripuranthagan, T. Vembuli, S. Kumaravel, E. Erusappan, E. Chicardi, S. Chinnasamy, Detoxification of harmful pollutants using highly efficient visible light active Ru/TiO_2/PVDF photocatalytic membranes, Mater. Res. Bull. 167 (2023) 112421, https://doi.org/10.1016/j.materresbull.2023.112421.
[61] A. Baral, D.P. Das, M. Minakshi, M.K. Ghosh, D.K. Padhi, Probing environmental remediation of RhB organic dye using α-MnO_2 under visible- light irradiation: structural, photocatalytic and mineralization studies, ChemistrySelect. 1 (2016) 4277–4285, https://doi.org/10.1002/slct.201600867.
[62] S.Y. Xiong, X.H. Liu, X.J. Zhu, G. Liang, Z.J. Jiang, B.S. Cui, J.H. Bai, One-step preparation of well-dispersed spindle-like Fe_2O_3 nanoparticles on g-C_3N_4 as highly efficient photocatalysts, Ecotoxicol. Environ. Saf. 208 (2021) 111519, https://doi.org/10.1016/J.ECOENV.2020.111519.
[63] B. Krishnakumar, T. Imae, J. Miras, J. Esquena, Synthesis and azo dye photodegradation activity of ZrS_2–ZnO nano-composites, Sep. Purif. Technol. 132 (2014) 281–288, https://doi.org/10.1016/J.SEPPUR.2014.05.018.
[64] C. Li, S. Yu, H. Che, X. Zhang, J. Han, Y. Mao, Y. Wang, C. Liu, H. Dong, Fabrication of Z-scheme heterojunction by anchoring mesoporous γ-Fe_2O_3 nanospheres on g-C_3N_4 for degrading tetracycline hydrochloride in water, ACS Sustain. Chem. Eng. 6 (2018) 16437–16447, https://doi.org/10.1021/ACSSUSCHEMENG.8B03500/ASSET/IMAGES/MEDIUM/SC-2018-035008_0016.GIF.
[65] L. Wang, Y. Wang, X. Li, T. He, R. Wang, Y. Zhao, H. Song, H. Wang, 3D/2D Fe_2O_3/g-C_3N_4 Z-scheme heterojunction catalysts for fast, effective and stable photo Fenton degradation of azo dyes, J. Environ. Chem. Eng. 9 (2021) 105907, https://doi.org/10.1016/J.JECE.2021.105907.
[66] S. Suganthi, S. Vignesh, V. Raj, S. Manoharadas, S. Pandiaraj, H. Kim, Synergistic influence of vanadium pentoxide-coupled graphitic carbon nitride composite for photocatalytic degradation of organic pollutant: Stability and involved Z-scheme mechanism, Environ. Res. 231 (2023) 116288, https://doi.org/10.1016/J.ENVRES.2023.116288.

[67] P. Roy Chowdhury, H. Medhi, K.G. Bhattacharyya, C. Mustansar Hussain, Recent progress in the design and functionalization strategies of transition metal-based layered double hydroxides for enhanced oxygen evolution reaction: a critical review, Coord. Chem. Rev. 483 (2023) 215083, https://doi.org/10.1016/J.CCR.2023.215083.

[68] K. Balu, B. Avula, M. Durai, S. Kumaravel, E. Chicardi, R. Sepúlveda, E. Erusappan, I. Hasan, Y.H. Ahn, Fabrication of Bi_2O_3/bismuth titanates modified with metal-organic framework-In_2S_3/$CdIn_2S_4$ materials for electrocatalytic H_2 production and its photoactivity, Langmuir. 39 (2023) 15055–15066, https://doi.org/10.1021/acs.langmuir.3c02031.

[69] P. Sharma, M. Minakshi, J. Whale, A. Jean-Fulcrand, G. Garnweitner, Effect of the anionic counterpart: molybdate vs. tungstate in energy storage for pseudo-capacitor applications, Nanomaterials. 11 (2021) 580, https://doi.org/10.3390/nano11030580.

[70] T. Tran-Phu, R. Daiyan, J. Leverett, Z. Fusco, A. Tadich, I. Di Bernardo, A. Kiy, T. N. Truong, Q. Zhang, H. Chen, P. Kluth, R. Amal, A. Tricoli, Understanding the activity and stability of flame-made Co_3O_4 spinels: a route towards the scalable production of highly performing OER electrocatalysts, Chem. Eng. J. 429 (2022) 132180, https://doi.org/10.1016/j.cej.2021.132180.

[71] C. Wang, X. Du, X. Zhang, Controlled synthesis of W-Co3S4@Co3O4 as an environmentally friendly and low cost electrocatalyst for overall water splitting, Int. J. Hydrogen Energy. 48 (2023) 12739–12752, https://doi.org/10.1016/j.ijhydene.2022.12.241.